# Theoretical Studies of Low-frequency Alfvén Modes in Tokamak Plasmas

Ruirui Ma[1,4], W. Heidbrink[2], L. Chen[3,2,4], F. Zonca[4,3], and Z. Qiu[3,4]

[1]Southwestern Institute of Physics, P.O. Box 432, Chengdu, 610041, China

[2]Department of Physics and Astronomy, University of California, Irvine, CA 92697-4574, USA

[3]Institute for Fusion Theory and Simulation and Department of Physics, Zhejiang University, Hangzhou, 310027, China

[4]Center for Nonlinear Plasma Science and C.R. ENEA Frascati, C.P. 65, 00044 Frascati, Italy

This work is supported by the NSFC under Grant No. 12175053, and the ITER-CN under Grant No. 2018YFE0304103 and CREATE, EUROfusion Enabling Research Projects WP19-ER/ENEA-05.

3rd Trilateral International Workshop on Energetic Particle Physics, 7-10 Nov. 2022

核工业西南物理研究院 Southwestern Institute of Physics 中核集团 CNNC

# Low Frequency Continuous Spectrum

- The low frequency Alfvén wave (LFAW) continuous spectra are formed due to the coupling of Alfvén waves and acoustic waves.
- These Alfvén instabilities with frequencies near the kinetic thermal-ion gap [L.Chen & F.Zonca, 2007NF] can interact with both thermal and fast particles [F.Zonca et al 2010JPCS].

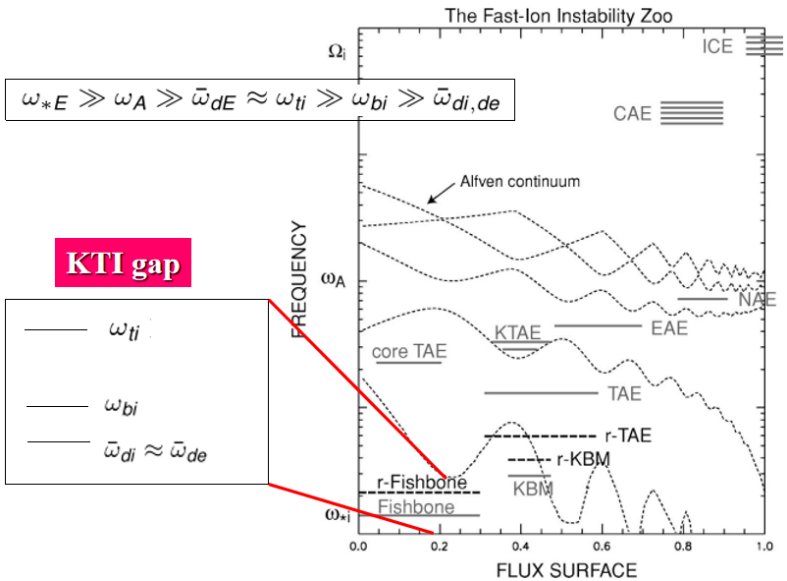


Figure 1: Schematic illustration of the approximate frequency, radial location and mode width of observed fast-ion driven modes vs. poloidal flux for a monotonically increasing $q$ profile. [Original figure from Ref. [Heidbrink et al 2002POP].

- The mode frequencies ($\omega$) are in the order of $\omega_{*pi}$ ($\propto n$), which may be comparable to ($\omega_{ti}$) or ($\omega_{bi}$);
- For $|\omega| \sim |\omega_{ti}|$ or $|\omega| \ll |\omega_{ti}|$, the thermal plasma compression effects play important roles in their D.R.[F. Zonca2007NF, Chavdarovski2009PPCF, Chen and Zonca, 2016RMP].

- Accurate treatment of low frequency spectrum requires kinetic theory considering the resonant interaction with thermal ions [N.Gorelenkov et al 2009POP].
- The low-frequency Alfvén instabilities include but are not limited to the KBM [Cheng1982, Tang1980], BAE [Heidbrink1993, Turnbull1993], AITG mode [Zonca1999, Zonca2009] and BAAE [Gorelenkov2007, Gorelenkov2009, Zonca2010];

## LFAM instabilities in DIII-D experiments [Heidbrink et al 2021NFa&b&c]

- These LFAMs are relevant to the recent DIII-D experiments with and without EPs [Heidbrink2021NFa&b&c, Du et al., 2021PRL]; provides the primary motivation.

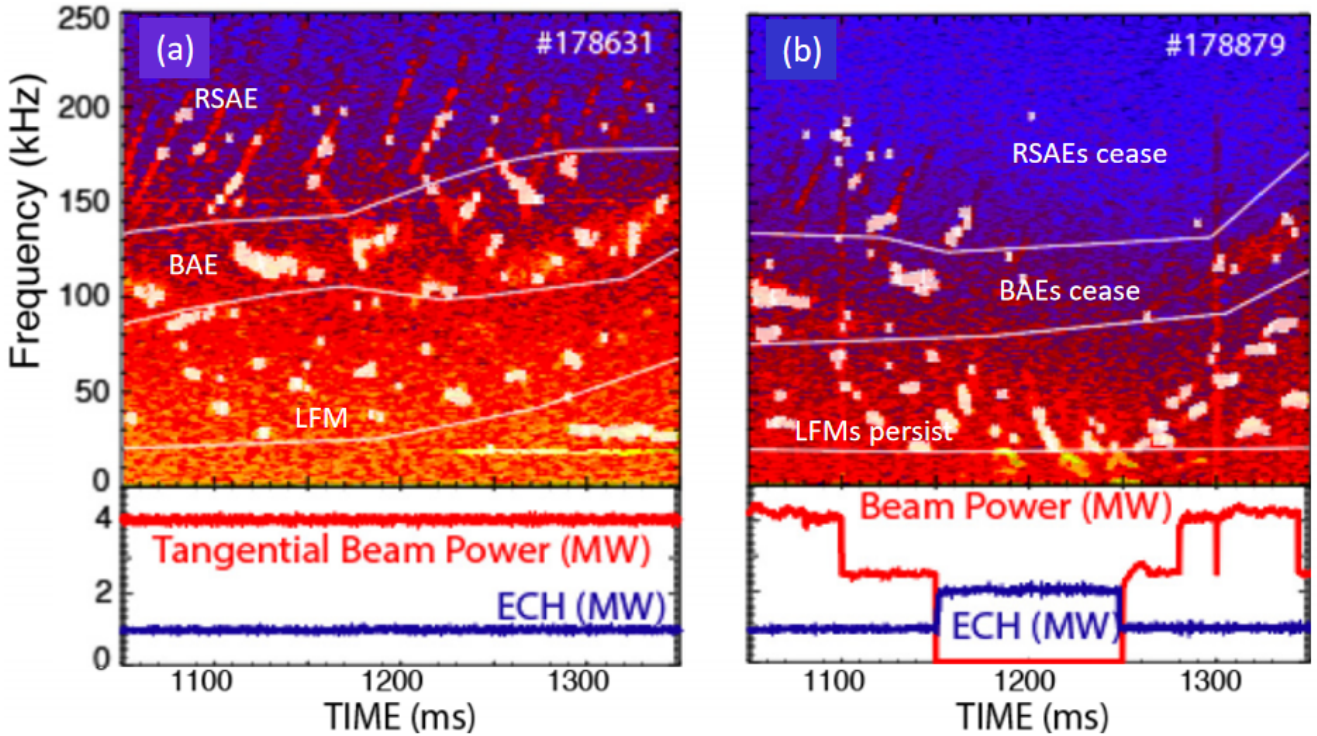


Figure 2: Experimental results presented in Ref. [Heidbrink et al 2021NFa]. Time evolution of the ECE spectra, neutral beam power, and ECH power.

- RSAEs, BAEs and LFMs are excited with NBI; RSAEs and BAEs disappear after turning-off beams, LFMs persist.
- Both RSAEs and BAEs are excited by energetic ions; while energetic ions are unimportant in LFM destabilization [W. Heidbrink2021NFa,b].

# LFAM instabilities in DIII-D experiments [Heidbrink et al 2021NFa&b&c]

- Unstable modes occur when $q_{min}$ approaches a rational value;
- Large $T_e$ or its gradient is essential for instabilities;
- The modes in the ascending pattern of higher frequency BAEs and LFMs is separated by approximately $f_{rot}$.

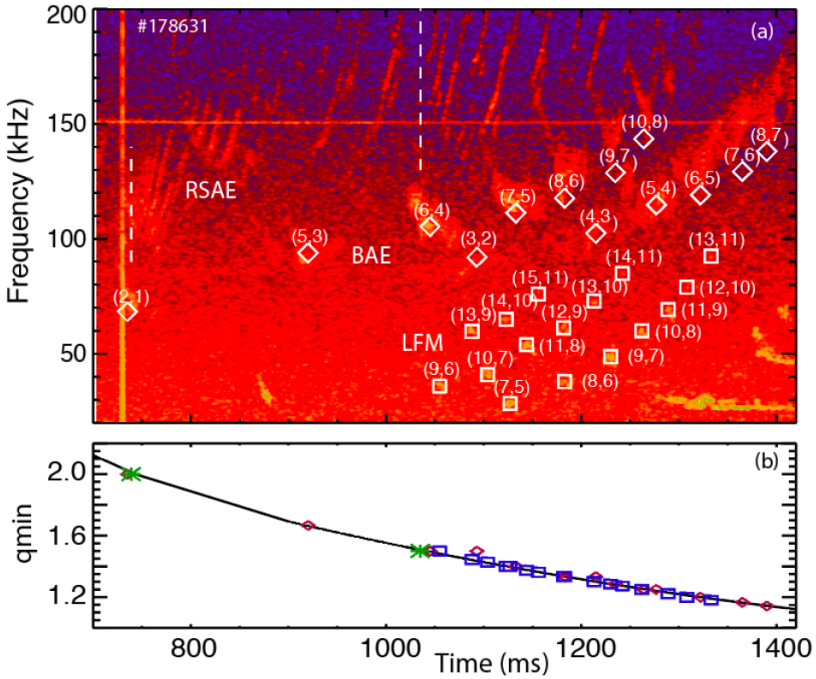


- For LFMs, the mode freq. is low in the plasma frame, in the range of diamagnetic frequencies; the maximum freq. occurs at rational values of $q_{min}$; exhibit 'Christmas lights' and 'mountain peaks' spectral patterns as $q_{min}$ evolves [Heidbrink2021NFa];
- For BAEs, they occur at times near rational values of $q_{min}$ but the timing of unstable modes is less precise than for LFMs [Heidbrink2021NFb];

Figure 3: Experimental results presented in Ref. [Heidbrink et al 2021NFb-Fig.8]. (a) ECE spectra, (b) $q_{min}$ vs. time for DIII-D discharge #178631. The BAE (diamond) and LFM (square) symbols represent the values of $m/n$ shown on the spectrogram.

- Theoretical prediction [L.Chen 2020Private notes, Heidbrink2021NFa] and simulation studies (FAR3D & GTC) [Varela2018,Choi2021]: LFMs is a low-freq. reactive instability of predominately Alfvénic polarization.
- This work $\Rightarrow$ applying the **theoretical framework of the GFLDR** to capture the nature of the instabilities and explain the exp. observations.

## Profiles of DIII-D #178631@1200ms

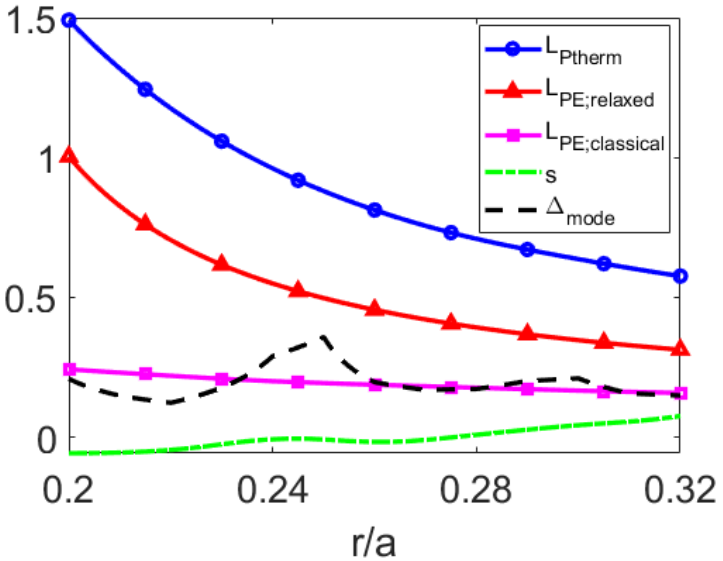


Figure 4: The radial dependences of the typical scale lengths of thermal and energetic particle pressure gradients, as well as the magnetic shear and the estimated radial mode width. Acknowledge W. Heidbrink and the DIII-D team for providing DIII-D equilibrium data of shot #178631.

- $L_P = -P/(\partial P/\partial r)$: the typical scale length of pressure gradient;
- The relaxed EP profile provided with EFIT reconstruction; the classical EP profile obtained using TRANSP/NUBEAM;
- $\Delta_m \simeq 1/|nq''(k_{||n0}q_0R_0)|^{1/2}$: the radial width of the mode for weak and/or vanishing magnetic shear [Zonca2002 POP].

- For LFMs, the instability has nothing to do with EPs [Ma et al 2022PPCF]:
  - $L_{Pth} \gg \Delta_m$: the moderate equilibrium pressure gradient case, $\Rightarrow$ the usual local limit of the GFLDR for the mode [Zonca2000 POP];
- For BAEs, the instability is driven by EPs:
  - $L_{PE;relaxed} > \Delta_m$: the moderate equilibrium pressure gradient case, $\Rightarrow$ the usual local limit of the mode dispersion relation;
  - $L_{PE;classical} \sim \Delta_m$: a direct investigation of the global DR. [Zonca2000 POP].

核工业西南物理研究院 Southwestern Institute of Physics 中核集团 CNNC

## The local general fishbone-like dispersion relation for LFAMs

- When $s = 0$ at one isolated singular layer but $S \equiv (r/q)[q'']^{1/2}$ does not vanish, the local GFLDR [Zonca2002, Zonca2007, Zonca2014a&b, Chen2017] $\Rightarrow$

$$iS(\Lambda_n^2 - k_{\|n0}^2 L_0^2)^{1/2}(1/n)^{1/2}\left[k_{\|n0}L_0 - i(\Lambda_n^2 - k_{\|n0}^2 L_0^2)^{1/2}\right]^{1/2} = \delta\hat{W}_{nf} + \delta\hat{W}_{nk}(\omega), \tag{1}$$

  - $\Lambda_n(\omega)$: the generalized inertia response to the short radial length-scale "singular" region;
  - $\delta\hat{W}_{nf}$ and $\delta\hat{W}_{nk}$: the "fluid" and "kinetic" potential energy in the "regular" ideal region.
  - $k_{\|n0} = (nq_{min} - m)/q_{min}R_0$; $L_0 \simeq qR_0$;
  - The finite $k_{\|n0}L_0$ plays an important stabilizing role; finite line bending effect at $r = r_0$.

- In low-$\beta$ ($\beta = 8\pi P/B_0^2 \approx \epsilon^2$) axisymmetric tokamak plasmas, for LFAMs with the inclusion of diamagnetic effects & kinetic effects of circulating and trapped particle dynamics [Chavdarovski and Zonca 2009]

$$\Lambda_n^2 = I_\phi\left[\frac{\omega^2}{\omega_A^2}\left(1 - \frac{\omega_{*pi}}{\omega}\right) + \Lambda_{cir}^2 + \Lambda_{tra}^2\right], \tag{2}$$

- $\mathfrak{S} \equiv (i\delta E_\| / k_\|)_{a.c.}/\delta\phi_{d.c.}$: a measure for the electrostatic component of the mode polarization.
  - $a.c.$ and $d.c.$: the sinusoidal and nearly constant (flute-like) components of the quantities [L. Chen and F. Zonca 2017].
  - $|\mathfrak{S}| \ll 1$: the typical SAW polarization; $|\mathfrak{S}| \sim 1$: a mixed Alfvénic and acoustic polarization.
- The explicit expressions of $\Lambda_n^2$ and $\mathfrak{S}$ are given in Refs. [Chavdarovski and Zonca,2009&2014].

$$\delta\hat{W}_{nf} \simeq \frac{\pi}{4}\left(\frac{S^2 k_{\|0}q_0R_0}{n} - \frac{3}{2}\alpha^2 S\left|\frac{k_{\|0}q_0R_0}{n}\right|^{1/2} + \frac{9}{32}\alpha^4\right) \tag{3}$$

- Assuming anisotropic slowing-down beam ion dist. function with a single pitch angle ($\lambda = \mu/\varepsilon$):

$$F_{0E} = \frac{B_0\beta_E(r)}{2^5\sqrt{2}\pi^2 m_E\varepsilon_b}\sqrt{(1 - \lambda_0 B_0)}\varepsilon^{-3/2}\delta(\lambda - \lambda_0) \tag{4}$$

$$\delta\hat{W}_{nku} \simeq \frac{\pi\alpha_E(r)}{2^{5/2}}(1 - \lambda_0 B_0/2)\bar{\omega}\left[2 - \bar{\omega}\ln\left(\frac{\bar{\omega}+1}{\bar{\omega}-1}\right)\right]; \text{ with } \bar{\omega} = \omega/\omega_{tE} \tag{5}$$

## The global dispersion relation for LFAMs

- Closely following Refs. [F. Zonca et al., 2000POP & 2002POP], the low frequency vorticity equation for the $(m, n)$ mode reads

$$(\mathbf{e}_\theta - \mathbf{e}_r\xi)\cdot\left[\Lambda^2 - \Omega_{A,m}^2\left(1+\frac{x^2}{\Omega_{A,m}}+\frac{x^4}{4\Omega_{A,m}^2}\right)\right](\mathbf{e}_\theta - \mathbf{e}_r\xi)\delta\phi_m + E_t\delta\phi_m = 0, \tag{6}$$

  - $\mathbf{e}_r$ and $\mathbf{e}_\theta$: the radial and poloidal unit vectors;
  - $x^2 = nq_0''(r-r_0)^2$, $\xi \equiv (i/n^{1/2})S(\partial/\partial x)$;
  - $\Omega_{A,m} \equiv k_{\|n0}q_0R_0 = (nq_0 - m)$ the normalized parallel wave vector;
  - $E_t$: the fluid-like particle and energetic ion contributions;
  - $\delta\phi_m$: the $m$th poloidal harmonic of the scalar field perturbation.
- In particular, the normalized pressure gradient of EPs with classical profiles obeys

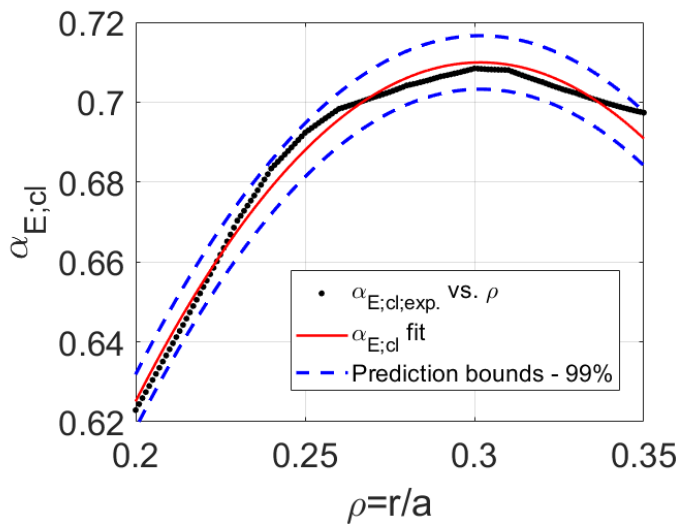


$$\alpha_E(\rho) = C_1\left(1 - \frac{(\rho - C_2)^2}{C_3^2}\right), \tag{7}$$

with $C_1 = 0.7099$, $C_2 = 0.3018$ and $C_3 = 0.2944$.

The maximum drive of EPs locates at $\rho = 0.3018$, which deviates from the radial position of $q_{min}$.

Figure 5: The radial dependence of the normalized pressure gradient of EPs with the classical profile. Here, the radial position of $q_{min}$ is $\rho_0 = 0.28$.

- We have

$$\alpha_E(r) = \delta_a \alpha_{E0}(1 - \frac{(r - r_0 + \delta_b)^2}{\delta_c^2 L_{PE;cl}^2}), \tag{8}$$

- with $\delta_a = C_1/\alpha_{E0}$, $\delta_b = r_0 - C_2 a$ and $\delta_c = C_3 a/L_{PE;cl}$; $a$ is the minor radius; $\alpha_{E0}$ and $L_{PE;cl}$ are evaluated at $r = r_0$.
- Introducing the notation $x = r - r_0 = \lambda z - \delta_b$, Eq. (6) is readily cast into the form

$$\begin{aligned} &\frac{\partial^2}{\partial z^2}\delta\phi_m - \frac{n\lambda^2}{S^2}\left(1 - \frac{\delta\hat{W}_{f0} + \frac{2\delta_a}{\pi}\delta\hat{W}_{ku0}}{\epsilon_{A0}}\right)\delta\phi_m - \frac{1}{4}z^2\delta\phi_m = 0, \\ &\frac{2n\lambda^4\delta_a\delta\hat{W}_{ku0}}{\epsilon_{A0}\pi S^2\delta_c^2 L_{PE;cl}^2} = \frac{1}{4}, \end{aligned} \tag{9}$$

  - with $\epsilon_{A0} = \Lambda^2 - \Omega_{A,m}^2$, $\delta\hat{W}_{f0} = \frac{1}{2}D_S^2 - \frac{3}{4}\alpha^2 D_S + \frac{9}{64}\alpha^4$, $\delta\hat{W}_{ku0} = \frac{\pi\alpha_{E0}}{4\sqrt{2}}\left[2 - \bar{\omega}\ln\left(\frac{\bar{\omega}+1}{\bar{\omega}-1}\right)\right]$, and $D_S = S\sqrt{\Omega_{A,m}/n}$.
- Equation (9) yields the following global D.R. for LFAMs excited by EPs,

$$\frac{-n^{1/2}\pi^{1/2}\delta_c L_{PE;cl}\epsilon_{A0}^{1/2}}{2\sqrt{2}S\delta_a^{1/2}\delta\hat{W}_{ku0}^{1/2}}\left(1 - \frac{\delta\hat{W}_{f0} + \frac{2\delta_a}{\pi}\delta\hat{W}_{ku0}}{\epsilon_{A0}}\right) = 2L + 1, \text{ the radial mode number L=0,1,2,3 ...} \tag{10}$$

- The eigenfunctions are obtained from the exponential behavior:

$$\delta\phi_m(r) \propto H_L(z)e^{-z^2} \Rightarrow \exp\left(-\frac{(r - r_0 + \delta_b)^2}{4\lambda^2}\right), \tag{11}$$

  - $H_L(z)$ represents $L$th order Hermite polynomials;
  - The typical radial width ($w$) of $\delta\phi_m$: $w^2 = 4\lambda^2$.

# Numerical studies of LFAM instabilities

- Referring to the DIII-D #178631 experiment at the time $t = 1200$ ms [W. Heidbrink et al., 2021NFa], the $q$-profile has a reversed shear configuration with $q_{min} = 1.3765$ at $r_0/a = 0.28$ and $q_{min}$ decreases from 1.49 to 1.18 in the time window 1050 ms $< t <$ 1350 ms.

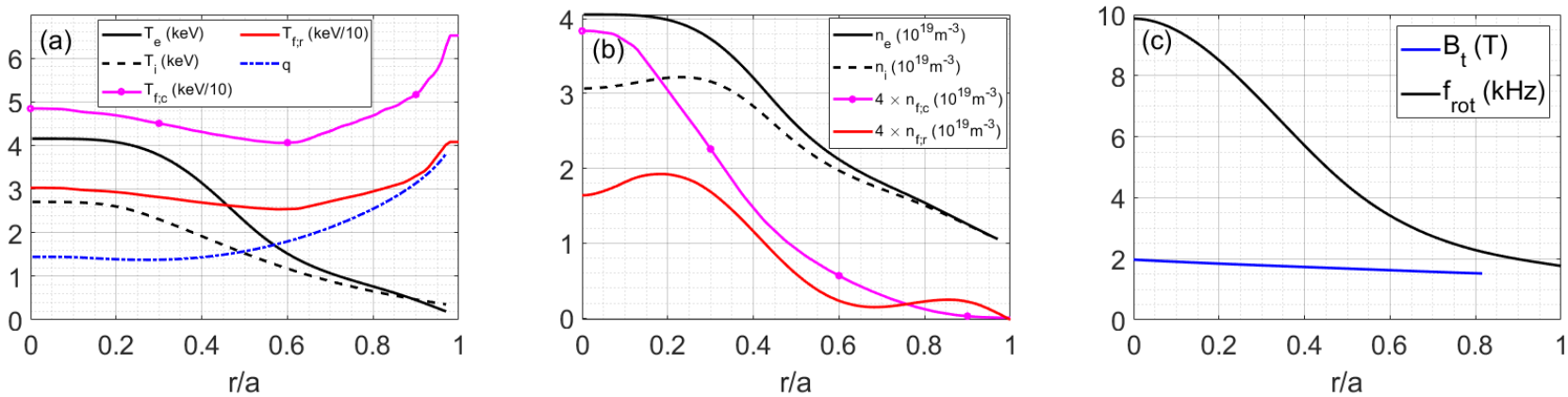


Figure 6: Radial profiles of temperature (density) of thermal particles and energetic ions, as well as the $q$, $B_t$ and the rotation frequency $f_{rot}$ of DIII-D shot #178631 at 1200 ms. (Acknowledge W. Heidbrink and the DIII-D team for providing DIII-D equilibrium data of shot #178631).

The linear properties of LFAMs without EPs by solving the local GFLDR; $L_{Pth} \gg \Delta_m$;

The linear properties of LFAMs with the $\begin{cases} \text{relaxed EP profiles by solving the local GFLDR} & L_{PE;relaxed} > \Delta_m, \\ \text{classical EP profiles by solving the global GFLDR} & L_{PE;classical} \sim \Delta_m. \end{cases}$

## Identification of LFMs observed in DIII-D – the local GFLDR without EPs [Ma, Chen, Zonca et al., 2022PPCF]

- $\eta_i \equiv L_{ni}/L_{Ti} = 0$ and $\delta\hat{W}_{nf} = 0$;

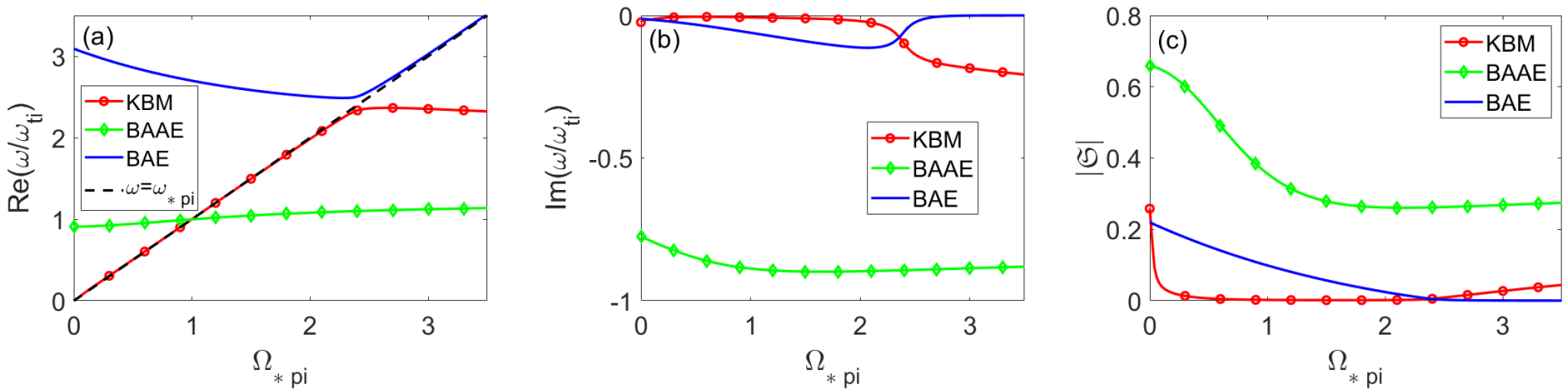


Figure 7: The dependence of the real frequencies, the growth rates and the polarization of modes on $\Omega_{*pi} \equiv \omega_{*pi}/\omega_{ti}$ with $\eta_i = 0$ and $\delta\hat{W}_{nf} = 0$.

- The three stable branches: the KBM ($\omega \sim \omega_{*pi}$), the BAE ($\omega/\omega_{ti} \simeq q_0\sqrt{7/4+\tau}$), and the BAAE (a frequency of half of the BAE; strong damping);
- A mode crossing occurs with increase of $\omega_{*pi}$; a switch of mode properties occurs after mode coupling;
- The KBM and BAE: essentially of Alfvénic polarization; BAAE: significant electrostatic component.

- $\eta_i = 0$ and $\delta\hat{W}_{nf}$ is given by Eq. (3); ($\delta\hat{W}_{nf} = -0.0041$).

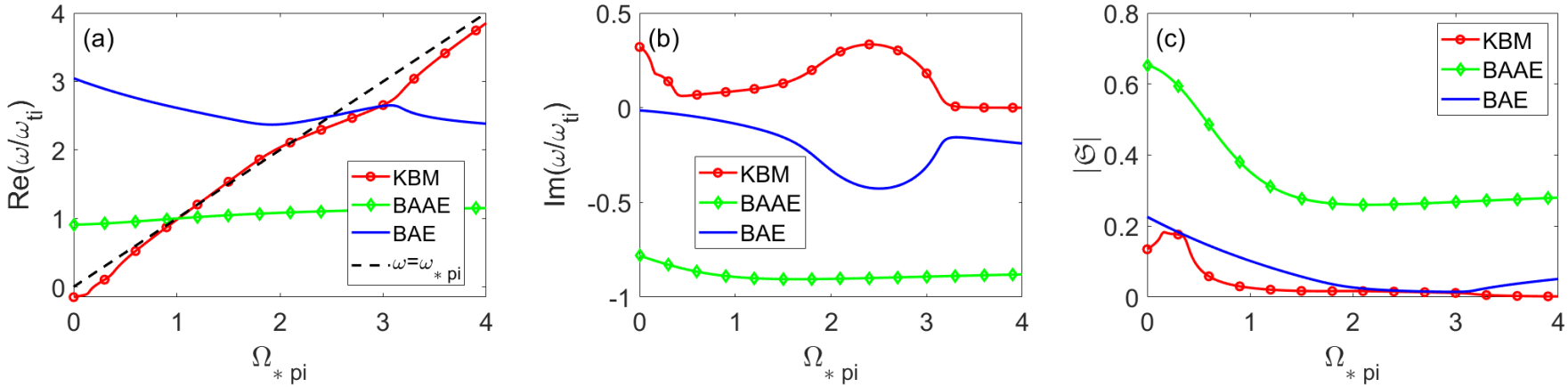


Figure 8: The dependence of the real frequencies, the growth rates and the polarization of modes on $\Omega_{*pi} \equiv \omega_{*pi}/\omega_{ti}$ with $\eta_i = 0$ and $\delta\hat{W}_{nf} \neq 0$.

- The negative $\delta\hat{W}_{nf}$ changes the topology of the dispersion curves.
- The KBM is unstable in both low ($|\omega| \ll \omega_{ti}$) and high ($|\omega| \gtrsim \omega_{ti}$) frequency regions.
- For $|\omega| \gtrsim \omega_{ti}$,
  - (i) the unstable KBM is always accompanied by a damped BAE having an approximately complex conjugate frequency;
  - (ii) the polarizations of the two modes are identical.

  essential features of linear reactive instability.
- For $\eta_i = 0$ case, there is no coupling between KBM and BAAE.

- $\eta_i \neq 0$ and $\delta\hat{W}_{nf} \neq 0$ (adopt the local equilibrium parameters of the DIII-D discharge #178361)

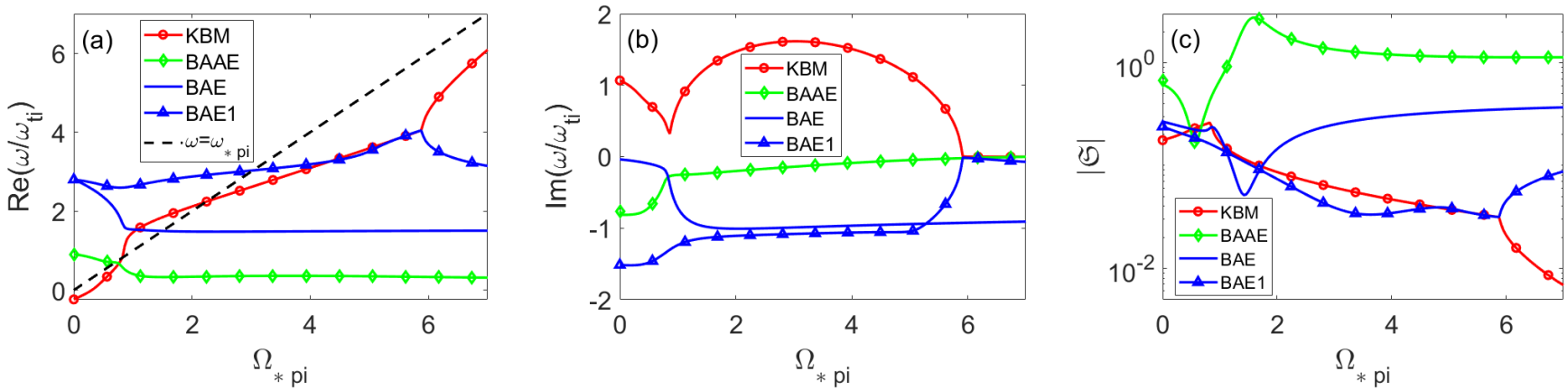


Figure 9: The dependence of (a) mode frequencies, (b) growth rates and (c) polarization of modes on $\Omega_{*pi} \equiv \omega_{*pi}/\omega_{ti}$ with $\delta\hat{W}_{nf} \neq 0$.

- The KBM freq. always scales with $\omega_{*pi}$; unstable in both low ($|\omega| \ll |\omega_{ti}|$) and high ($|\omega| \gtrsim |\omega_{ti}|$) freq. regions.
- For $|\omega| \ll \omega_{ti}$, the KBM freq. first increases and then couples with the BAAE and reduces the BAAE damping rate.
- For $|\omega| \gtrsim \omega_{ti}$, the KBM couples with the strongly damped BAE1 and reduces the BAE1 damping rate; the corresponding spectral features exhibit the typical of a coupled complex pair;
- BAAE: a mixed Alfvénic and acoustic polarization; both BAE and KBM: Alfvénic polarization.
- For DIII-D case, $\Omega_{*pi} = 0.313$, $f_{pl} \simeq 0.7$ kHz, the LFM observed in DIII-D is a reative-type unstable KBM with dominantly Alfvénic polarization.
- Remark: The coupling between KBM and BAAE is sensitive to $\eta_i$.

# Numerical studies of 'Christmas light' observation [Ma, Chen, Zonca et al., 2022PPCF]

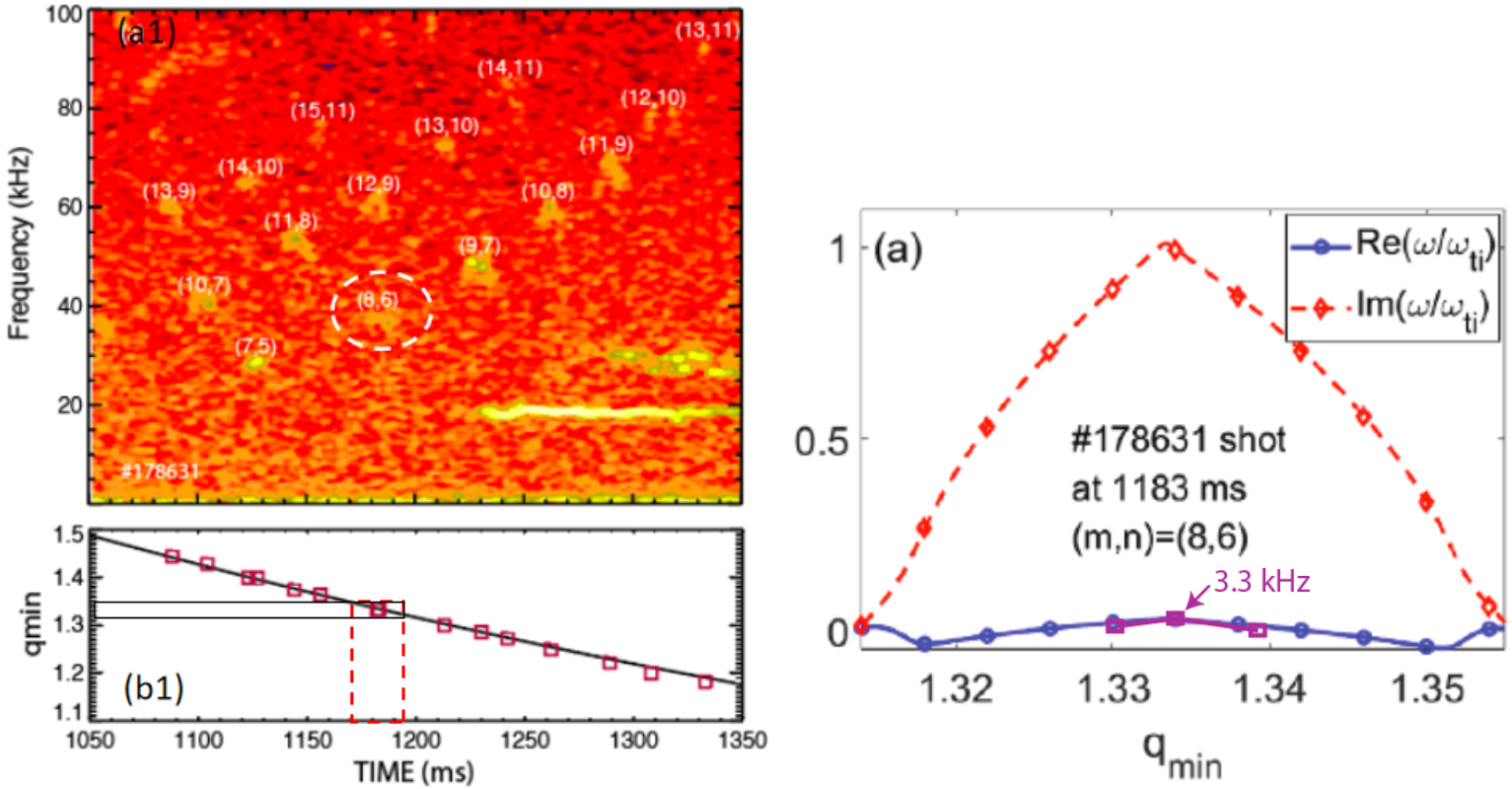


Figure 10: LHS: Experimental results presented in Ref. [Heidbrink et al 2020NFa], (a1) ECE spectra from channels and (b1) $q_{min}$ vs. time for DIII-D discharges #178631; RHS: The dependence of mode frequencies and growth rates on $q_{min}$ for the 'Christmas light' pattern.

- The freq. has a weak dependence on $q_{min}$; stays approximately 0;
- The instabilities are peaked at $q_{min}$ being a rational number ($k_{||n0} = 0$), and quickly quenched by the finite $|k_{||n0}|$ field line bending term in Eq. (1).
- The unstable window in $q_{min}$ is rather narrow; the $\Delta q_{min}$ instability window corresponds to a short time window of about 15 ms; consistent with exp. observations.

# EP effects on the LFAM stability properties – With the relaxed EP profiles

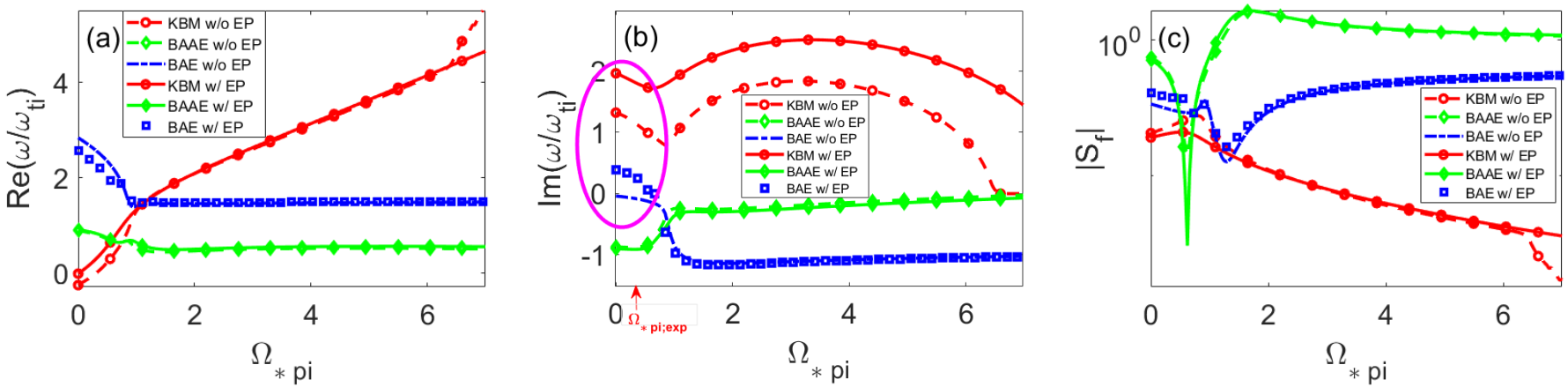


Figure 11: Dependences of (a) mode frequencies, (b) growth rates and (c) polarization of the modes on $\Omega_{*pi} \equiv \omega_{*pi}/\omega_{ti}$ for the cases w/o EPs (dashed curves with markers) and w/ EPs (solid curves with markers).

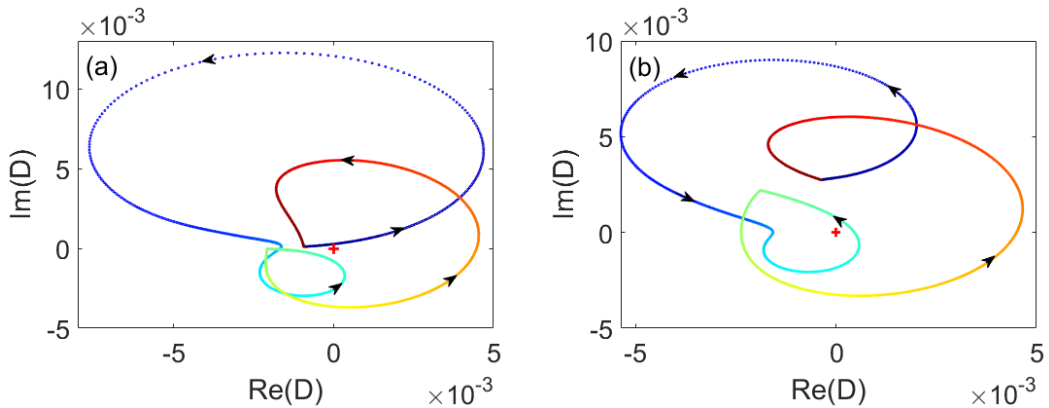


Figure 12: The Nyquist diagram in the complex $D(\omega)$ plane for the cases (a) without and (b) with EP effects.

- In the absence of EPs, the KBM is the only unstable mode; turning on EP effect, both the KBM and BAE are unstable in the low-frequency regime;
- The frequency of the KBM slightly increases in the presence of EPs; consistent with the exp. observations [Heidbrink et al 2021NFb].
- In this case, the stability of BAAE is not affected by EPs; consistent with the theoretical prediction in Ref. [Chen and Zonca 2017POP].

# EP effects on the LFAM stability properties – With the relaxed EP profiles

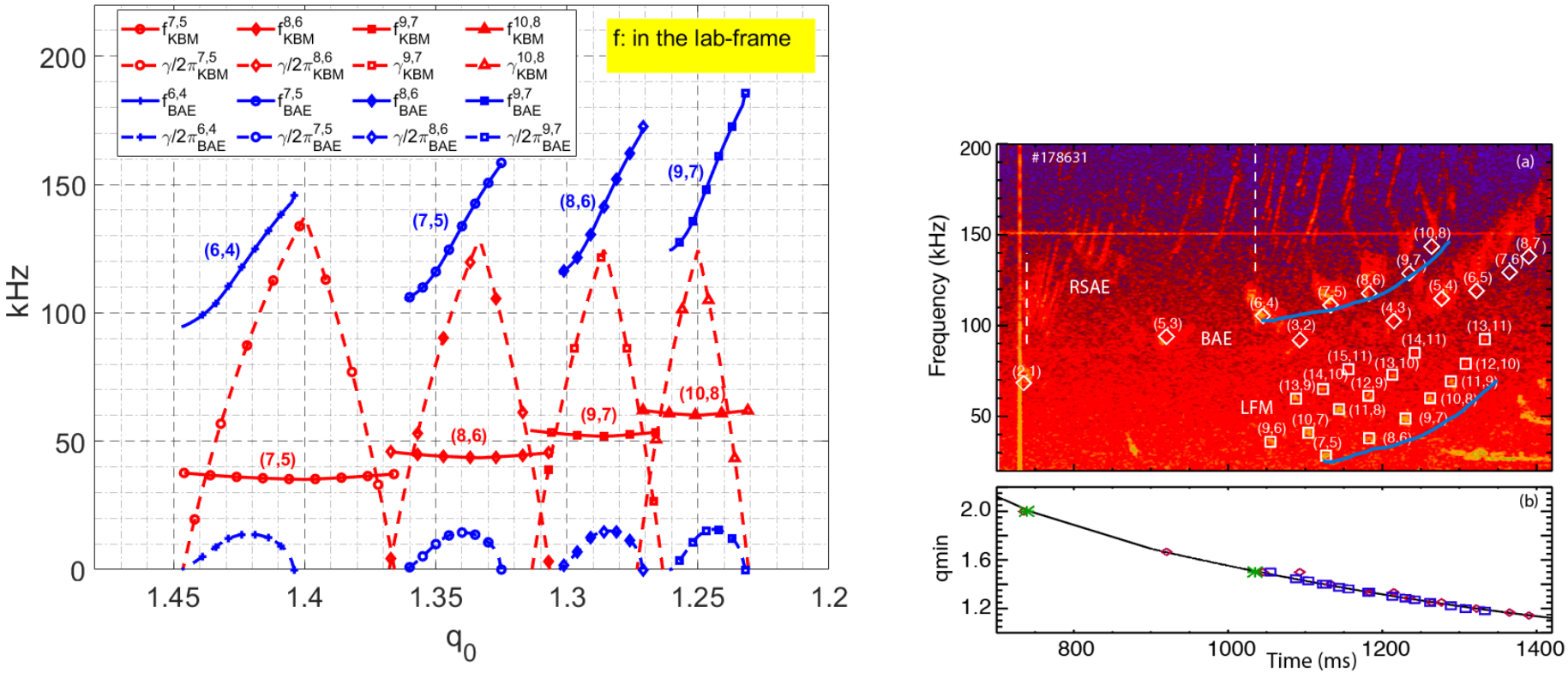


Figure 13: Dependences of mode frequencies (solid lines with markers) and growth rates (dashed lines with markers) on $q_{min}$ for KBMs (red curves) and BAEs (blue curves) for different ($m$, $n$).

The numerical analysis based on the GFLDR is in good agreement with the experimental results:

- BAEs occur at times near rational values of $q_{min}$ but the timing of unstable modes is less precise than for KBMs;
- The low-$n$ BAEs tend to deviate more from rational $q_{min}$ crossings than higher $n$ modes.
- The modes in the ascending pattern of higher frequency BAEs and lower frequency KBMs is separated by approximately $f_{rot}$ ($\sim$ 7.5 kHz).

## Theoretical understanding based on the GFLDR

1. For BAE with $|\omega| \gg |\omega_{ti}|$, $\Lambda^2 \simeq \frac{\omega^2-\omega_{BAE}^2}{\omega_A^2}$ with $\omega_{BAE}^2 = (7/4+\tau)(1+1/q_0^2)\upsilon_i^2/R_0^2$. Letting $\omega = \omega_r + i\gamma$ with $|\gamma/\omega_r| \ll 1$, i.e., assuming weakly unstable modes,

$$\omega_r^2 = \omega_{BAE}^2\left[1+\frac{\omega_A^2}{\omega_{BAE}^2}\left(\frac{n}{k_{\|n0}q_0R_0}\frac{\left(\delta\hat{W}_{nf}+\mathrm{Re}(\delta\hat{W}_{nk}(\omega_r))\right)^2}{S^2}+k_{\|n0}^2q_0^2R_0^2\right)\right], \tag{12}$$

$$\gamma = \mathrm{Im}(\delta\hat{W}_{nk}(\omega_r))\frac{\omega_A^2}{\omega_r}\frac{n\left(\delta\hat{W}_{nf}+\mathrm{Re}(\delta\hat{W}_{nk}(\omega_r))\right)}{k_{\|n0}q_0R_0S^2}, \tag{13}$$

- For gap mode BAE, the causality condition gives $\delta\hat{W}_{nf}+\mathrm{Re}(\delta\hat{W}_{nk}(\omega_r)) < 0$; EPs offer instability drive, i.e., $\mathrm{Im}(\delta\hat{W}_{nk}(\omega_r)) > 0$; the mode instability requires $k_{\|n0}q_0R_0 = nq_0 - m < 0$, e.g., the unstable (6,4) BAE occurs at $q_0 < 6/4 = 1.5$, (7,5) BAE occurs at $q_0 < 7/5 = 1.4$, etc., as shown in Fig. 13.
- The duration of different BAEs is influenced by the associated resonances with the EPs, as well as by the value of $q_{min}$.

2. For KBM (LFM) with $|\omega| \ll |\omega_{ti,bi}|$, $\Lambda^2 \simeq c_0\frac{q_0^2}{\sqrt{\epsilon}}\frac{(\omega-\bar{\omega}_{di})(\omega-\omega_{*pi})}{\omega_A^2}$, with $\bar{\omega}_{di}$ is the average thermal-ion precession frequency; $c_0 \simeq 1.6$ due to trapped and barely circulating particles [Rosenbluth1998,Graves2000].

$$\omega = \frac{1}{2}(\bar{\omega}_{di}+\omega_{*pi}) \pm \frac{1}{2}\left[(\omega_{*pi}-\bar{\omega}_{di})^2 - \frac{4\omega_A^2\sqrt{\epsilon}}{q^2c_0s^2}\left(\frac{n\left(\delta\hat{W}_{nf}+\mathrm{Re}(\delta\hat{W}_{nk}(\omega_r))\right)^2}{k_{\|n0}q_0R_0S^2} - k_{\|n0}^2q_0^2R_0^2\right)\right]^{1/2}, \tag{14}$$

and the system is reactively unstable if

$$\frac{|\omega_{*pi}-\bar{\omega}_{di}|^2}{\omega_A^2} < \frac{4\sqrt{\epsilon}}{q^2c_0}\left(\frac{n\left(\delta\hat{W}_{nf}+\mathrm{Re}(\delta\hat{W}_{nk}(\omega_r))\right)^2}{k_{\|n0}q_0R_0S^2} - k_{\|n0}^2q_0^2R_0^2\right). \tag{15}$$

- For KBM, $k_{\|n0}q_0R_0 \to 0$ gives the maximum drive for reactive-type instability.

## EP effects on the LFAM stability properties – With the classical EP profiles

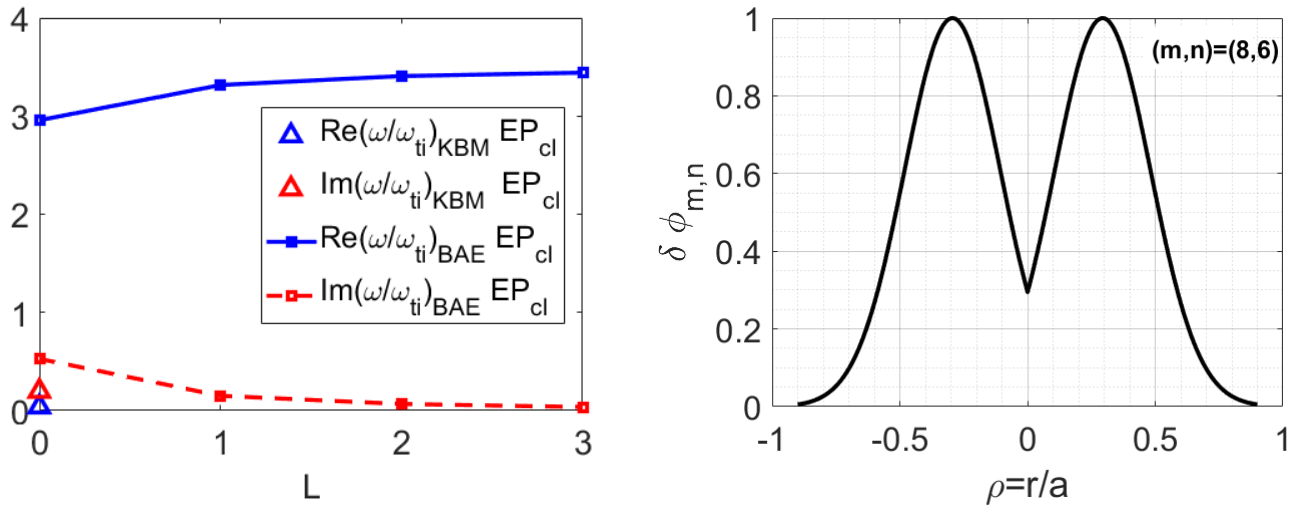


Figure 14: LHS: The dependences of the frequencies (blue marker or curve) and growth rates (red marker or curve) of the KBM (triangle markers) and BAE (line with markers) on the radial mode number $L$. The parameters are evaluated at $r = r_0$ and (m,n)=(8,6). RHS: The radial mode structure $\delta\phi_{8,6}$(r) for the BAE.

- The ground eigenstate with $L = 0$ is most unstable for BAE and KBM;
- For BAE, $\omega/\omega_{ti} = 2.8075 + 0.5279i$; in the plasma frame: (80.6710 +15.1686i) kHz; $\gamma/\omega \simeq 0.19$; resonantly excited by EPs;
- For KBM, $\omega/\omega_{ti} = -0.1115 + 0.1972i$; in the plasma frame: (-3.2031 + 5.6658i) kHz; $|\gamma/\omega| \simeq 1.8 \gg 1$; reactive-type instability.
- For $L = 0$, the radial eigenfunction of BAE - $\delta\phi_m \propto \exp\left(-\frac{(|r|-r_0+\delta_b)^2}{4\lambda^2}\right)$; a Gaussian with a shape similar to the experimentally observed; with $\delta b = r_0 - 0.1932 = -0.014$;
- $L_{PE;classical} = 0.1773 \lesssim \Delta_m = 2\lambda = 0.2107$;
- The BAE radially peaks at $\rho = (r_0 - \delta_b)/a = 0.3018$, i.e., the radial position of maximum instability drive from EPs; see Fig. (5) and Eq. (8).
- It can be expected that the radial mode structure of the KBM should peak at the rational value of $q_{min}$ where the instability drive reaches the maximum.

## Continuum spectra for LFAMs: $\Lambda_n^2(\omega) = k_{\|n}^2 q^2 R_0^2 = (nq - m)^2$ [Zonca et al., 2010JPCS]

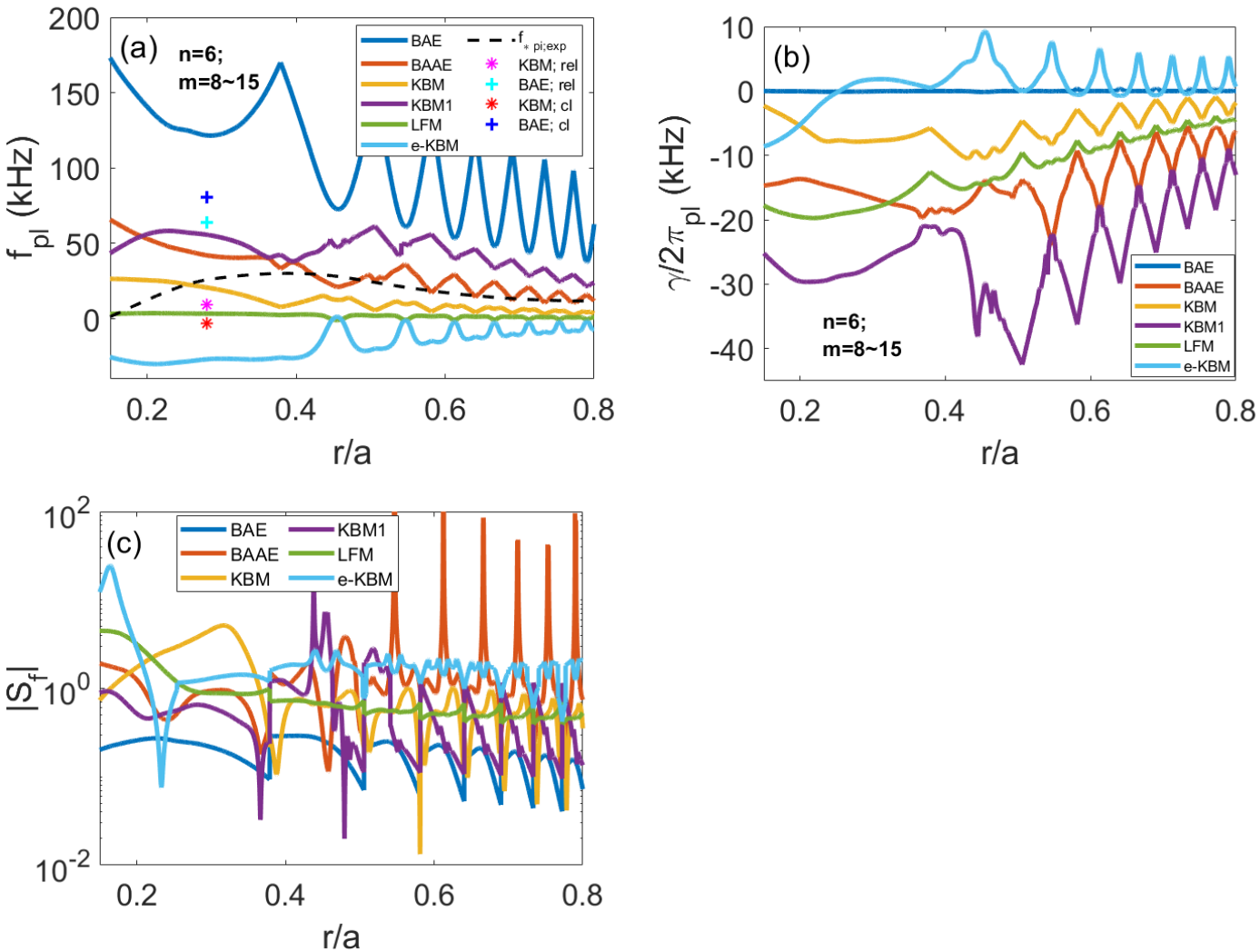


Figure 15: The continuum spectra of low-frequency Alfvén branches for n=6, m=8-15. The equilibrium profiles of DIII-D #178631 at 1200 ms are adopt.

- $\Lambda_n$ includes diamagnetic effects & thermal ion compressibility (well passing only) & DAW and DW sideband coupling effects [F. Zonca et al, 2010JPCS].

核工业西南物理研究院 Southwestern Institute of Physics 中核集团 CNNC

## Summary and Discussions

Applying the GFLDR, the essential features of LFAM instabilities observed in the experiments can be well captured.

- In the absence of EPs,
  - the LFM observed in DIII-D is a reactive unstable KBM with dominantly Alfvénic polarization;
  - Due to diamagnetic and trapped particle effects, the LFM(KBM) can be coupled with the BAAE in the low-frequency region ($|\omega| \ll |\omega_{ti}|$); or with the BAE in the high frequency region ($|\omega| \gtrsim |\omega_{ti}|$); resulting in reactive instability;
  - The ascending spectral patterns of LFAMs can be theoretically interpreted by varying $q_{min}$;
- In the presence of EPs,
  - Both LFMs and BAEs are unstable; while the BAAEs do not affected by EPs;
  - The experimental observations that BAEs occur at times near rational values of $q_{min}$ but the timing of unstable modes is less precise than for KBMs have been explained.

**Thanks for your attention!**